Focusing High Maneuvering Bistatic Forward-Looking SAR With Stationary Transmitter Using Extended Keystone Transform and Modified Frequency Nonlinear Chirp Scaling

Jiabao Ding, *Student Member, IEEE*, Yachao Li, *Member, IEEE*, Ming Li, *Member, IEEE*, and Jiadong Wang

***Abstract*—This article presents an imaging solution for high maneuvering bistatic forward-looking SAR with stationary transmitter (STHM-BFSAR). In STHM-BFSAR configuration that the transmitter is mounted on a stationary platform in side-looking mode while the receiver does high-speed maneuvering in forward-looking mode, high speed and acceleration induced by high dynamic characteristics of receiver in both along-track and height direction cause larger range cell migration (RCM) and more severe 2-D spatial variation of Doppler characteristics, which makes it more difficult to obtain well-focused bistatic SAR image. Furthermore, different from the general airborne bistatic SAR, STHM-BFSAR has a larger azimuth cubic phase term that exceeds $\pi/4$ rad, which seriously affects the image quality. To deal with these problems, an imaging algorithm based on extended keystone transform (EKT) and modified frequency nonlinear chirp scaling (FNCS) is proposed in this article. EKT can correct spatial variant range curvature and bulk linear RCM, and the residual RCM is smaller than traditional keystone transform. The proposed modified FNCS is used to equalize the azimuth-range-dependent Doppler parameters in the frequency domain, which produces lower side-lobes and higher accuracy by compensating for the second-order spatial variation of the azimuth cubic coefficients. The final simulation results in this article verify the effectiveness of the proposed algorithm.**

***Index Terms*—2-D spatial variation, extended keystone transform (EKT), frequency nonlinear chirp scaling (FNCS), high maneuvering bistatic forward-looking SAR with stationary transmitter (STHM-BFSAR).**

NOMENCLATURE

T	Transmitter.
R	Receiver.
$\mathbf{T}$	Location of the transmitter.
$\mathbf{R}_0$	Initial location of the receiver.
$\mathbf{V}_{R0}$	Velocity vector of the receiver.
$\mathbf{A}_R$	Acceleration vector of the receiver.
$\mathbf{P}(x_p, y_p, 0)$	Location of an arbitrary point target.
f_c	Carrier frequency.
$\hat{t}$	Fast time.
t_m	Slow time.
c	Speed of light.
γ	Chirp rate.
$k_i(R_{bf0})$	Expansion coefficient of slant range history.
$k_i(a; R_{bf0})$	Expansion coefficient coupled with the acceleration.
$k_i(v; R_{bf0})$	Expansion coefficient containing the velocity.
K_i	Expansion coefficient of the updated slant range history.
f_r	Range frequency.
f_a	Doppler frequency.
B_a	Doppler bandwidth.
f_n	Azimuth focusing position.
$H_{\mathrm{AC}}(f_r, t_m)$	Acceleration compensation function.
$H_{\mathrm{LWC,DCC}}(f_r, t_m)$	LRCM and DCC factor.
$H_{\mathrm{SRC,RCC}}(f_r, t_a)$	Phase compensation function.
$H_{\mathrm{AD}}(t_a)$	Phase adjustment factor.
$H_{\mathrm{AS}}(f_a)$	Fifth-order perturbation function.

Manuscript received August 24, 2021; revised November 16, 2021 and January 22, 2022; accepted February 15, 2022. Date of publication February 23, 2022; date of current version April 1, 2022. This work was supported in part by the National Key R&D Program of China under Grant 2018YFB2202500, in part by the National Natural Science Foundation of China under Grant 62171337, in part by the Key R&D Program of Shaanxi Province under Grant 2017KW-ZD-12, in part by the Shaanxi Province Funds for Distinguished Young youths under Grant S2020-JC-JQ-0056, in part by the National Natural Science Foundation of China under Grant 62101396, and in part by the Fundamental Research Funds for the Central Universities under Grant XJS212205. *(Corresponding author: Yachao Li.)*

Jiabao Ding, Yachao Li, and Ming Li are with the National Laboratory of Radar Signal Processing, Xidian University, Xi'an 710071, China (e-mail: 15091537475@163.com; ycli@mail.xidian.edu.cn; liming@xidian.edu.cn).

Jiadong Wang is with the Academy of Advanced Interdisciplinary Research, Xidian University, Xi'an 710071, China (e-mail: jiadongwang@xidian.edu.cn).

Digital Object Identifier 10.1109/JSTARS.2022.3153824

I. INTRODUCTION

WITH the development of radar technology, synthetic aperture radar (SAR) has been widely used in the military and civilian fields because it can obtain 2-D high-resolution images of static scene at long distances and under any weather conditions [1]–[5]. However, monostatic SAR cannot image the forward-looking area due to inherent geometric limitation, which restricts many scene applications, such as autonomous landing, autonomous navigation, and missile terminal guidance [6]–[8]. Due to the increasing demand in these applications, bistatic SAR (BiSAR) was proposed. BiSAR separates the receiver and transmitter at different spatial locations to prevent azimuth ambiguity making it possible to image the

forward-looking area, which is generally called bistatic forward-looking SAR (BFSAR). High maneuvering bistatic forward-looking SAR with stationary transmitter (STHM-BFSAR) is a BiSAR system with a complex configuration, which can realize guided missile detection and silent strike at low cost. In this special configuration, transmitter is mounted on a stationary platform in side-looking mode and receiver is mounted on a high maneuvering platform with curve track in forward-looking mode. The existence of high forward-looking angle and high speed and acceleration makes range and azimuth coupling more severe, so that traditional BiSAR imaging algorithms based on the linear trajectory model are no longer applicable [9]. The existing literature on BiSAR includes space–time–frequency synchronization [10], [11], imaging mechanism [12], imaging algorithm [13]–[16], and experiment [17], [18]. This article focuses on the imaging algorithm problem of STHM-BFSAR.

Since BiSAR system was proposed, many imaging algorithms have been developed to obtain well-focused SAR images for subsequent target recognition and matching. Generally, these methods can be divided into three types: time domain algorithm (TDA), frequency domain algorithm (FDA), and wavenumber domain algorithm (WDA). TDA mainly refers to back projection algorithm (BPA) and its improved form, fast factorized BP (FFBP) [19]–[21]. BPA is considered an ideal focusing method in any configuration due to the absence of approximate assumptions. However, the huge computational complexity limits its application on high maneuvering platforms due to real-time processing requirements. FFBP reduces the amount of calculation but at the expense of accuracy. For the time being, time domain imaging algorithms are not yet suitable for application to high maneuvering platforms. FDA is an imaging method with both high efficiency and precision, especially suitable for real-time processing. The common FDA includes range-Doppler (RD) algorithm [22], chirp scaling algorithm, nonlinear chirp scaling (NCS) algorithm, and modified NCS [23]–[26], etc. In the early stage, FDA pays more attention to the acquisition of 2-D spectrum in order to better apply RDA to BiSAR. Due to the existence of double-square-root term or higher order terms in the range history, BiSAR generally uses Loffeld's bistatic formula [27], [28] and the method of series reversion (MSR) [29] to obtain the spectrum of the echo signal instead of the traditional POSP [30]. Then, design range compression (RC), range cell migration correction (RCMC), and secondary range compression (SRC) filters based on the obtained high-precision 2-D spectrum. In [31] and [32], bistatic airborne SAR processing strategies based on RDA are proposed. Li *et al.* [33] proposed an improved RD algorithm for spaceborne BiSAR. This method reduces the phase error introduced by the root term expansion, and has good focusing performance for space-borne BiSAR. However, none of these methods consider the spatial variation of the Doppler coefficient. NCS [34] is often used to equalize azimuth-range-dependence of azimuth frequency modulation (FM) rate term to achieve azimuth identical focusing. J *et al.* [35], [36] proposed an extended NCS for BFSAR and used keystone transform (KT) to correct range cell migration (RCM). The disadvantage of this method is that it does not consider the spatial variation of higher order phase terms, which usually cannot be ignored in STHM-BFSAR. Mei *et al.* [37] proposed a frequency domain algorithm, which compensates for the first-order spatial variation of azimuth cubic phase terms by constructing a perturbation function in the frequency domain. This is a wise method to focus the BiSAR data, but in the STHM-BFSAR configuration, this first-order approximation of the higher order phase term is not sufficient because the presence of high speed and acceleration will cause the residual phase error to be greater $\pi/4$ rad. WDA uses interpolation operations to achieve spectrum regularization and azimuth compression. This type of algorithm is generally more accurate than RD and NCS, but the complex and inefficient interpolation also limits its application and development.

In STHM-BFSAR mode, this special configuration will bring about two main problems. The first one is that the different dynamic characteristics of receiver and transmitter will make the coupling between range and azimuth more serious, so RCMC will be a challenge task. The other is the 2-D spatial variation of Doppler parameters caused by the lack of azimuth translation invariance, and the range position offset after RCMC will aggravate the variation. In recent years, some scholars have conducted research on BFSAR with stationary transmitter (ST-BFSAR) [38]–[40] and put forward some innovative ideas. But these methods are mostly aimed at airborne BiSAR. Chen *et al.* [41], proposed a new imaging method for missile-borne ST-BFSAR, which uses the linear RCMC (LRCMC) factor constructed from the center point of the scene and the NCS operation to complete the 2-D focus. This method also does not consider the spatial variation of azimuth higher order phase term, which causes the side-lobes elevation and side-lobes asymmetry of the SAR image.

Based on previous research and existing problems, we propose a new solution for STHM-BFSAR. First, the echo signal characteristics are analyzed based on the established geometric configuration and signal model of STHM-BFSAR. Preprocessing operation is done to remove the effect of acceleration on the 2-D spectrum. Second, LRCMC and Doppler centroid compensation (DCC) combined with the second-order KT are performed in the range frequency domain and azimuth time domain. Then, a higher order polynomial fitting method (HPF) is used to eliminate the spatial variation of the residual RCM. These three steps are called extended keystone transform (EKT). Third, the range dependence of Doppler parameters is removed based on the HPF results. After that, polynomial approximation of azimuth FM rate term and azimuth cubic term are obtained by numerical fitting. At last, the fifth-order perturbation function is used to perform the frequency nonlinear chirp scaling (FNCS) operation to eliminate the second-order spatial variation of the azimuth FM rate term and azimuth cubic phase term. Compared with the existing algorithms, the algorithm proposed in this article has the following innovative ideas: 1) EKT is introduced to realize the spatial variant RCMC, which includes spatial variant range curvature correction and bulk LRCMC. Compared with the traditional KT, the residual RCM of this method is smaller, which indicates a better RC effect and facilitate the subsequent azimuth focusing processing. 2) For the first time,

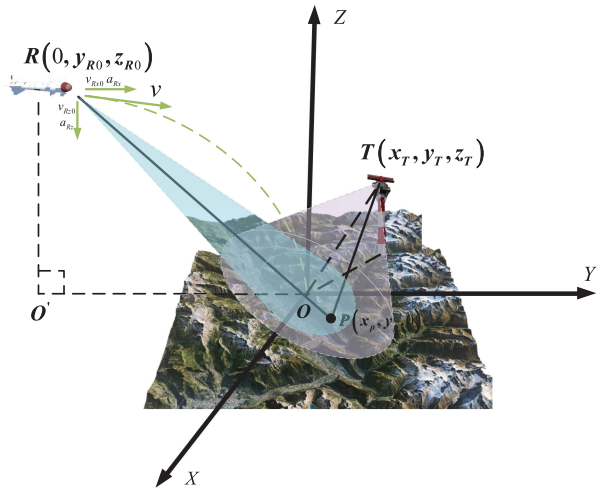

Fig. 1. Geometry configuration of STHM-BFSAR.

the second-order spatial variation of the azimuth cubic phase that cannot be ignored in STHM-BFSAR is taken into consideration. The third-order filter in the azimuth time domain combines with the fifth-order perturbation function to simultaneously eliminate the second-order spatial variation of the azimuth FM rate and azimuth cubic coefficients, which is more precise than traditional NCS.

The rest of this article is organized as follows. Section II describes the imaging geometry and echo signal model of STHM-BFSAR. Section III shows the procedures of the proposed algorithm in detail. The simulation experiment results are given in Section IV. Finally, Section V concludes this article.

II. Geometry and Signal Model

A. Signal Model

The geometry configuration of STHM-BFSAR is shown in Fig. 1, where the system of coordinate is denoted by (X, Y, Z), Y-axis coincides with the receiver's speed in along-track direction, Z-axis is perpendicular to the ground, and X-axis conforms to the right-hand rule. The transmitter T is mounted on a stationary high tower in side-looking mode located at $\mathbf{T} = (x_T, y_T, z_T)$. The receiver R makes a descending motion with curve track on the yoz-plane in forward-looking mode at the initial location $\mathbf{R}_0 = (0, y_{R0}, z_{R0})$, and the three-axis initial velocity vector and acceleration vector are $\mathbf{V}_{R0} = (0, v_{Ry0}, v_{Rz0})$ and $\mathbf{A}_R = (0, a_{Ry}, a_{Rz})$, respectively. The lavender region is the transmitter beam illumination scope, the light blue area is the receiver beam pointing scope, and the center of the beam overlap area is the origin of the coordinate system O. P is an arbitrary point target in the imaging area whose coordinate is denoted by $\mathbf{P}(x_p, y_p, 0)$. O' is the nadir point of the receiver's initial location.

The bistatic instantaneous slant range history is the sum of the slant range history from two platforms to point target P, defined as

$$R_T = \left[(x_T - x_p)^2 + (y_T - y_p)^2 + (z_T - z_p)^2\right]^{\frac{1}{2}}$$

$$R_R = \sqrt{x_p^2 + \left(y_{R0} + v_{Ry0}t_m + \tfrac{1}{2}a_{Ry}t_m^2 - y_p\right)^2 + \left(z_{R0} + v_{Rz0}t_m + \tfrac{1}{2}a_{Rz}t_m^2\right)^2}$$

$$R_{\text{bf}}(t_m) = R_T + R_R \tag{1}$$

where t_m is the slow time, and R_T and R_R are instantaneous slant range from the transmitter and receiver to the point target P, respectively. Considering the higher order terms introduced by the receiver acceleration, the range history should first be expanded to the fourth order at $t_m = 0$ by Taylor series [42]. Then, we have

$$R_{\text{bf}}(t_m) \approx R_{\text{bf0}} + \sum_{i=1}^{4} k_i \left(R_{\text{bf0}}\right) t_m^i \tag{2}$$

where R_{bf0} is the bistatic slant range at $t_m = 0$ and $k_i(R_{bf0}) = (1/i!)(d^i R_{\text{bf}}(t_m)/dt_m^i)|_{t_m=0}$ denotes the ith order derivative at $t_m = 0$, and the detailed expression formula can be obtained in [41]. The envelope and phase errors caused by the fourth-order Taylor expansion are less than a range resolution cell and $\pi/4$ rad, respectively, so it meets the imaging requirements.

Assuming that the signal sent by the transmitter is a linear frequency modulation (LFM) pulse, the echo signal reflected from point target after demodulation is

$$S_1(\hat{t}, t_m) = w_r\left(\hat{t} - \frac{R_{\text{bf}}(t_m)}{c}\right) w_a(t_m) \cdot \exp\left(j\pi\gamma\left(\hat{t} - \frac{R_{\text{bf}}(t_m)}{c}\right)^2\right) \exp\left(-j2\pi\frac{f_c}{c}R_{\text{bf}}(t_m)\right) \tag{3}$$

where w_r and w_a are the range and azimuth envelopes, respectively, $\hat{t}$ is the fast time, c is the speed of light, f_c is the carrier frequency, and γ is the chirp rate.

B. Echo Signal Characteristic Analysis

Due to the unique geometrical configuration of STHM-BFSAR and the different dynamic characteristics of the transmitter and receiver, it is necessary to analyze the echo signal characteristics of STHM-BFSAR before imaging algorithm design. Suppose that there are six points A, B, C, D, E, and F on the ground, as shown in Fig. 2(a). In order to show more intuitively, the receiver moves in a straight line at a constant speed in the forward direction. In the monostatic SAR configuration, points A, B, and C fall in the same range bin after processing compression due to the same beam center slant distance. Points D, E, and F have the same properties. However, in BFSAR with stationary transmitter, the range history is determined by the sum of the distance from the target to the receiver and the distance from the target to the transmitter. Therefore, point targets located in the same range bin in monostatic SAR will fall into different range bins due to different transmitter slant distances, as shown in Fig. 2(b). Points B and D are located in the same range bin, and they have different RCM and Doppler characteristics due to the inherent range-dependent nature of monostatic SAR, well as C and E, which is caused by the

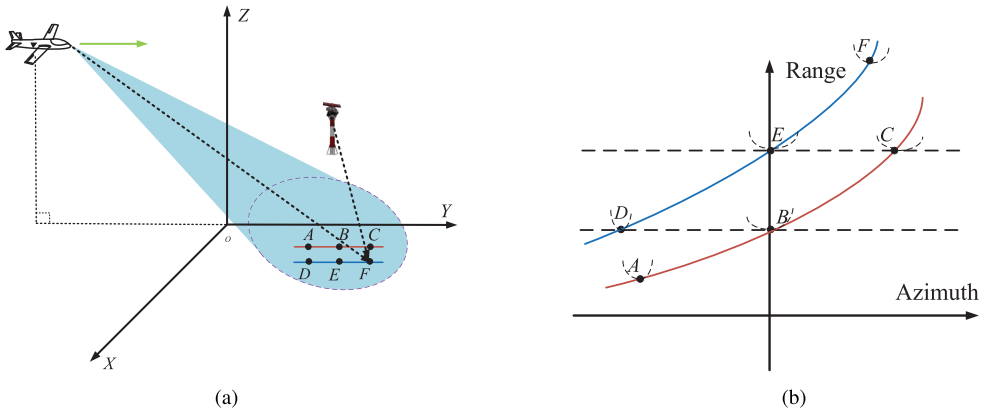

Fig. 2. Analysis of spatial variation characteristics caused by configuration. (a) Six points distributed on the ground plane. (b) Points represent the range gates in the time domain.

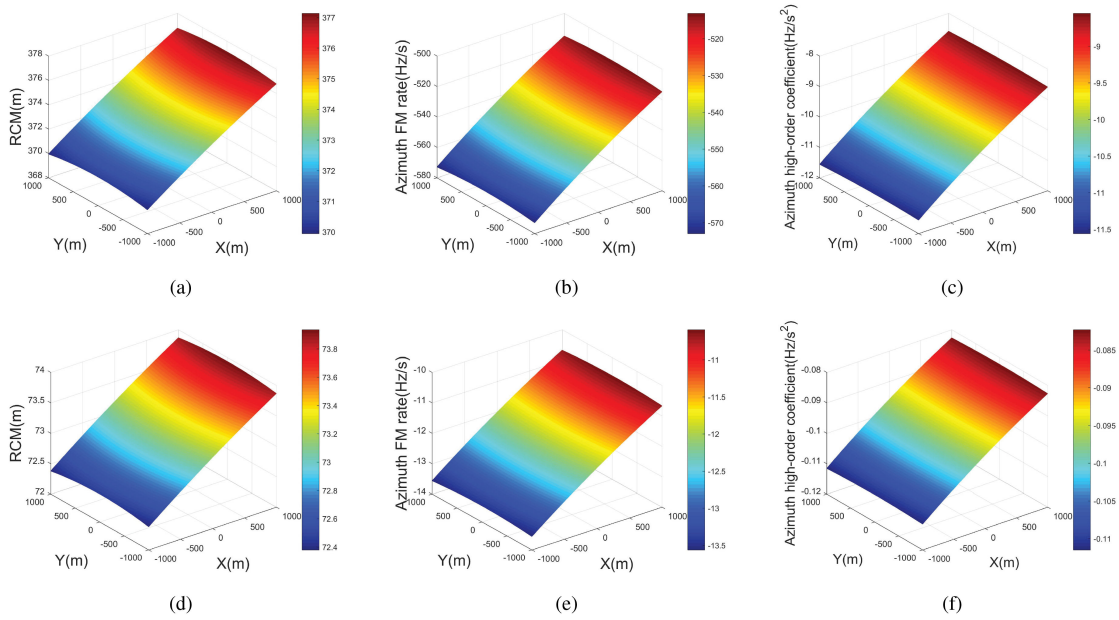

Fig. 3. Spatial variation characteristics of RCM and Doppler parameters. (a)–(c) Spatial variation characteristics of RCM, azimuth FM rate, and azimuth higher order coefficient in STHM-BFSAR. (d)–(f) Spatial variation characteristics of RCM, azimuth FM rate, and azimuth higher order coefficient in airborne ST-BFSAR without acceleration and descent velocity.

inherent properties of the system configuration. In STHM-BFSAR, the high maneuverability of the platform combined with the inherent properties of the geometric configuration will aggravate the degree of spatial variation of Doppler parameters, which seriously challenges imaging processing. Fig. 3 shows the different RCM and Doppler parameter characteristics of STHM-BFSAR and airborne ST-BFSAR, which indicates that range-azimuth coupling and Doppler parameter spatial variation are more serious in STHM-BFSAR.

III. Proposed Algorithm

As abovementioned, for STHM-BFSAR data processing, the main challenge tasks are RCMC and equalization of azimuth-range-dependent Doppler parameters. In STHM-BFSAR case, the RCM of the target caused by the change of the slant range sum from the two platforms to the target is 2-D spatial variant, which will cause serious coupling between azimuth and range. In this section, EKT is introduced to eliminate the 2-D spatial variant characteristics of RCM, which includes three main steps. The first step is to multiply the echo by the LRCMC factor to reduce the cross coupling. The second step is to use the second-order KT to eliminate the spatial variation of range curvature. The last step is the residual RCMC based on HPF in the range frequency and azimuth time domain. After that, the derivation of the proposed modified FNCS algorithm will be discussed in detail. In order to allow identical azimuth compression processing, modified FNCS is applied to equalize the FM rates and azimuth cubic phase along each range cell. The flowchart of the proposed algorithm is shown in Fig. 5.

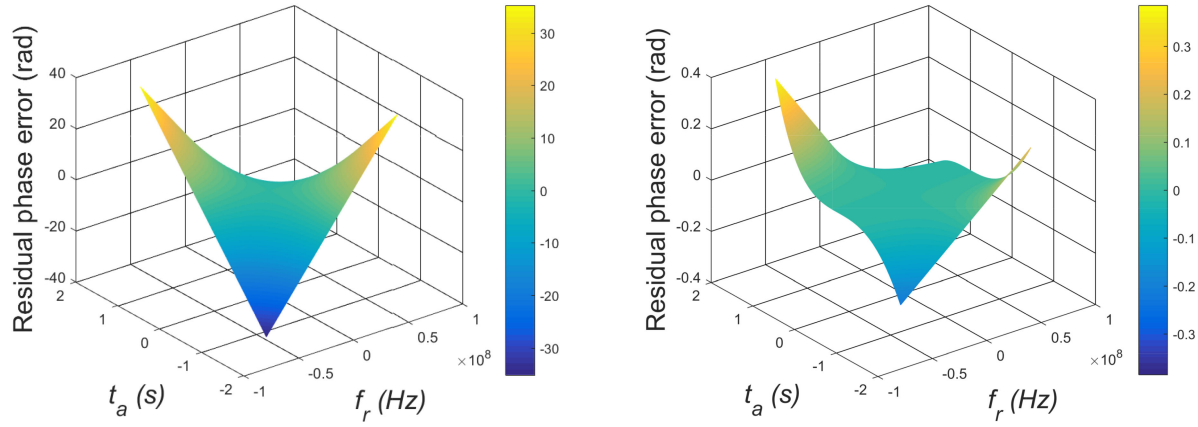

Fig. 4. Residual phase error. (a) Before HPF. (b) After HPF.

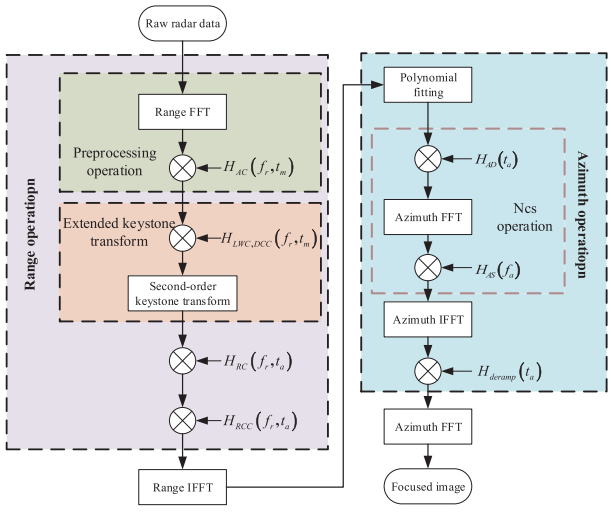

Fig. 5. Flowchart of the proposed algorithm.

A. Range Processing via EKT Operation

In STHM-BFSAR, the presence of acceleration in both along-track and vertical direction will negatively affect the azimuth resolution and the 2-D spectrum of the bistatic target. This effect exists in the azimuth FM rate that is coupled with the acceleration term, which will seriously degrade the image quality. Therefore, in order to avoid the impact of acceleration on imaging, we learn from the method in monostatic SAR to compensate for this term before the azimuth processing. First, substituting in (2) using follow expression

$$k_i(R_{\text{bf0}}) = k_i(a; R_{\text{bf0}}) + k_i(v; R_{\text{bf0}}) \tag{4}$$

where $k_i(a; R_{\text{bf0}})$ denotes the expansion coefficient coupled with the acceleration, and $k_i(v; R_{\text{bf0}})$ denotes the coefficient containing only the velocity component.

Then, transform received echo signal $S_1(\hat{t}, t_m)$ into range frequency domain by fast Fourier transform (FFT) on fast time variable $\hat{t}$, and construct the acceleration compensation function $H_{\text{AC}}(f_r, t_m)$ by taking the scene center as the reference point

$$S_1(f_r, t_m) = W_r(f_r)\, w_a(t_m) \exp\left(-j\pi \frac{{f_r}^2}{\gamma}\right) \cdot \exp\left(-j2\pi \frac{f_c + f_r}{c} R_{\text{bf}}(t_m)\right) \tag{5}$$

$$H_{\text{AC}}(f_r, t_m) = \exp\left(j2\pi \frac{f_c + f_r}{c} \sum_{i=2}^{4} k_i(a; R_{\text{ref}})\, t_m^i\right) \tag{6}$$

where f_r is the range frequency, $W_r(f_r)$ represents the range frequency envelope, and R_{ref} is the reference slant range at the center of the scene.

Multiplying (5) and (6) yields

$$S_2(f_r, t_m) = W_r(f_r)\, w_a(t_m) \cdot \exp\left(-j\pi \frac{{f_r}^2}{\gamma}\right) \exp\left(-j\Phi_1(f_r, t_m)\right) \tag{7}$$

where $\Phi_1(f_r, t_m)$ is shown in (8).

After the acceleration compensation operation, the impact of acceleration on imaging will be greatly alleviated, which is conducive to subsequent processing.

$$\Phi_1(f_r, t_m) = 2\pi \frac{f_c + f_r}{c} \left(\begin{array}{l} R_{\text{bf0}} + k_1(R_{\text{bf0}})\, t_m + \\ \sum_{i=2}^{4} \left(k_i(v; R_{\text{bf0}}) + k_i(a; R_{\text{bf0}})\right) t_m^i \\ - \sum_{i=2}^{4} k_i(a; R_{\text{ref}}) t_m^i \end{array} \right) \tag{8}$$

1) LRCMC and DCC by Linear Factor Multiplication: Due to the large forward-looking angle, the Doppler centroid deviates from the zero frequency, which may cause the azimuth spectrum to be blurred, and LRCM of the target is very serious in STHM-BFSAR. In order to alleviate this situation, we implement LRCM and DCC in the range frequency and azimuth time domain.

LRCMC and DCC factors are given by

$$H_{\mathrm{LWC,DCC}}(f_r,t_m)=\exp\left(j2\pi\frac{f_c+f_r}{c}k_1\left(R_{\mathrm{ref}}\right)t_m\right) \quad (9)$$

where $k_1(R_{\mathrm{ref}})$ is the range walk rate of the center point of the scene.

Multiplying (7) and (9), we can get the updated slant range expression, that is

$$R(t_m,R_{\mathrm{bf0}})=R_{\mathrm{bf0}}+\sum_{i=1}^{4}K_i t_m^i \quad (10)$$

where $K_i{=}k_i(v;R_{\mathrm{bf0}}){+}k_i(a;R_{\mathrm{bf0}}){-}k_i(a;R_{\mathrm{ref}})(i{=}2,3,4)$.

2) Second-Order KT for Range Compression: After LRCMC, the bulk linear RCM is corrected, and the first-order coupling of range and azimuth is reduced. However, due to the 2-D spatial variation characteristics of RCM, the farther away from the scene center, the larger the residual RCM. Therefore, the traditional LRCMC method using linear RCM of the scene center is not enough. In addition, the bulk LRCMC operation make the absolute value of K_1 smaller than that of K_2. A larger absolute value of K_2 indicates a more significant component in the RCM [36], [37]. Here, we introduce a second-order KT to remove the spatial variant range curvature. The second-order KT is performed by

$$t_m=\sqrt{\frac{f_c}{f_c+f_r}}t_a \quad (11)$$

where t_a is the slow time variable after the second-order KT. The phase term after the second-order KT is given by

$$\Phi_{\mathrm{KT}}(f_r,t_a)=-2\pi\frac{f_c+f_r}{c}R_{\mathrm{bf0}}- \left(\begin{array}{l}2\pi\frac{\sqrt{f_c(f_c+f_r)}}{c}K_1t_a+2\pi\frac{f_c}{c}K_2t_a^2+\\ 2\pi\frac{f_c}{c}\sqrt{\frac{f_c}{f_c+f_r}}K_3t_a^3+2\pi\frac{f_c}{c}\frac{f_c}{f_c+f_r}K_4t_a^4\end{array}\right). \quad (12)$$

Observing (12), the main part of the residual RCM, namely the second-order coupling of the range frequency variable f_r and the azimuth time variable t_a, is compensated.

3) Residual RCMC Based on HPF: In order to implement residual RCMC, the second term in (12) is expanded by the fourth-order Taylor series as follows:

$$\Phi_3\left(f_r,t_a\right)\approx\Phi_{30}+\Phi_{31}f_r+\Phi_{32}f_r^2 \quad (13)$$

where

$$\left\{\begin{array}{l}\Phi_{30}=2\pi\frac{f_c}{c}K_1t_a+2\pi\frac{f_c}{c}K_2t_a^2+2\pi\frac{f_c}{c}K_3t_a^3+2\pi\frac{f_c}{c}K_4t_a^4\\ \Phi_{31}=\pi\frac{K_1}{c}t_a-\pi\frac{K_3}{c}t_a^3-2\pi\frac{K_4}{c}t_a^4\\ \Phi_{32}=-\pi\frac{1}{4cf_c}K_1t_a+\pi\frac{3}{4cf_c}K_3t_a^3+\pi\frac{2}{cf_c}K_4t_a^4.\end{array}\right. \quad (14)$$

Inspecting (13), the first term contains azimuth modulation information and it is independent of the range frequency variable f_r. The second term is the first-order term of range frequency f_r, which is the residual RCM. The last term is the second-order coupling term of the range frequency variable f_r corresponding to SRC. Because the spatial variation of the slant range coefficient is mainly caused by its change with range, in order to select a suitable reference for SRC and RRC compensation, the method of polynomial fitting is used to eliminate the spatial variation of the fourth-order Taylor expansion coefficient

$$\left\{\begin{array}{l}K_1=K_{10}+K_{11}\left(\Delta r\right)+K_{12}(\Delta r)^2+K_{13}(\Delta r)^3\ldots\\ K_2=K_{20}+K_{21}\left(\Delta r\right)+K_{22}(\Delta r)^2+K_{23}(\Delta r)^3\ldots\\ K_3=K_{30}+K_{31}\left(\Delta r\right)+K_{32}(\Delta r)^2+K_{33}(\Delta r)^3\ldots\\ K_4=K_{40}+K_{41}\left(\Delta r\right)+K_{42}(\Delta r)^2+K_{43}(\Delta r)^3\ldots\end{array}\right. \quad (15)$$

where K_{10}, K_{20}, K_{30}, and K_{40} are the Taylor expansion coefficients corresponding to the center of the scene, respectively, K_{1i}, K_{2i}, K_{3i}, and K_{4i} $(i=1,2,3,\ldots,N$, where N is the fitting order) are the fitting coefficients, and Δr is the slant range difference of any point in the scene relative to the scene center. Fig. 4(a) illustrates the residual phase error before and after HPF. It can be seen that the residual phase error is greater than the phase error threshold rad due to the spatial variation of the residual RCM. By HPF, the Talor coefficients related to the scene can be obtained, and the residual phase error is less than rad, which indicates that the spatial variation of the residual RCM has been corrected, as shown in Fig. 4(b). After HPF operation, the phase compensation function combined with RC operation is expressed as

$$H_{\mathrm{SRC,RRCMC}}\left(f_r,t_a\right)=\exp\left(j\pi\frac{f_r^2}{\gamma}\right)\exp\left(j\Phi_{32}f_r^2+j\Phi_{31}f_r\right). \quad (16)$$

After the residual RCMC, the echo in the 2-D time domain is

$$S_3(\hat{t},t_a)=\sin c\left(B_r\left(\hat{t}-R_{\mathrm{bf0}}\right)\right)w_a\left(t_a\right) \cdot\exp\left(-j2\pi\frac{f_c}{c}\left(K_1t_a+K_2t_a^2+K_3t_a^3+K_4t_a^4\right)\right). \quad (17)$$

From (17), we can find that targets with the same R_{bf0} are in the same range cell gate. The third term represents the azimuth phase that has not been changed after EKT. Since the range processing corresponds to the range resolution cell, and the azimuth phase is related to the wavelength, the azimuth phase is more sensitive to errors. The detailed azimuth scaling processing procedures will be discussed in the next section. So far, we have completed the range processing of the STHM-BFSAR echo signal.

B. Azimuth Compression via Modified FNCS

Because the Taylor expansion coefficient of the slant range varies with different target coordinates, the 2-D spatial variation of the Doppler parameters cannot be ignored. However, the existing NCS method only considers the first-order spatial variation of the third-order azimuth coefficient at most, which is not sufficient in STHM-BFSAR because of the high speed and acceleration in both along-track and vertical direction. The residual phase error of the azimuth cubic phase term will cause the side lobes of the image to increase and reduce the azimuth focus depth. Therefore, in order to achieve the unified azimuth focusing processing, the spatial variation of the Doppler coefficient must be removed through the improved FNCS.

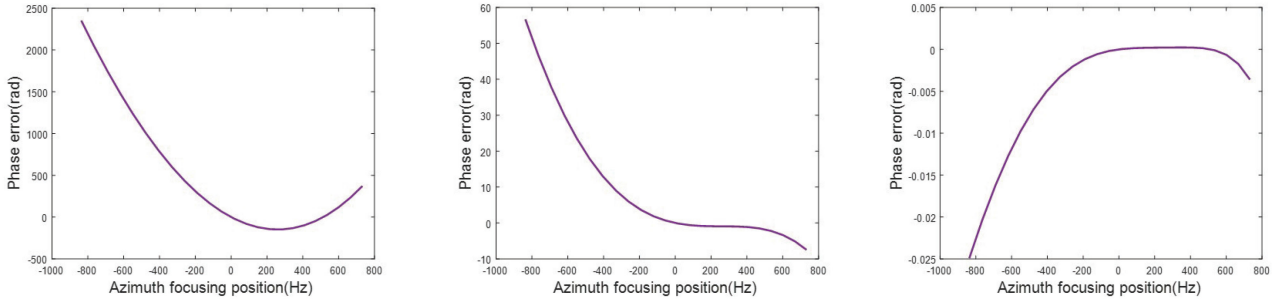

Fig. 6. Change curve of spatial variant azimuth phase error with different azimuth position. (a) Spatial variant azimuth phase error of $\phi_2(f_a, f_n)$. (b) Spatial variant azimuth phase error of $\phi_3(f_a, f_n)$. (c) Spatial variant azimuth phase error of $\phi_4(f_a, f_n)$.

There are mainly two existing azimuth NCS methods: time-domain NCS based on full-aperture data and frequency-domain NCS based on subaperture data, which correspond to the introduction of NCS factors in time and frequency domains, respectively. The time-domain NCS based on full-aperture data is not suitable for high-speed mobile platforms due to the large amount of data to be processed and ineffective for small-aperture imaging processing. For spotlight mode BFSAR imaging, the support regions of the target overlap in the slow time domain, but they are separated in the azimuth frequency domain, which provides support for the application of FNCS.

1) Analysis of Spatial Variation Characteristics of Azimuth Phase: First, we reexpress the phase term of (17) as follows:

$$\begin{aligned}\Phi_4\left(t_a; R_{\text{bf0}}, f_n\right) &= 2\pi f_{dc}\left(R_{\text{bf0}}, f_n\right) t_a + \pi f_{dr}\left(R_{\text{bf0}}, f_n\right) t_a^2 \\ &\quad + \pi f_{dk}\left(R_{\text{bf0}}, f_n\right) t_a^3 + \pi f_{dm}\left(R_{\text{bf0}}, f_n\right) t_a^4\end{aligned} \tag{18}$$

where $f_{dc}(R_{\text{bf0}}, f_n) = -K_1/\lambda$, $f_{dr}(R_{\text{bf0}}, f_n) = -2K_2/\lambda$, $f_{dk}(R_{\text{bf0}}, f_n) = -2K_3/\lambda$, and $f_{dm}(R_{\text{bf0}}, f_n) = -2K_4/\lambda$ are Doppler center, azimuth FM rate, azimuth cubic coefficient, and azimuthal quartic coefficient, respectively. These coefficients are expressed as a function of R_{bf0} and f_n, which also shows that they are 2-D spatially variant.

In monostatic SAR and airborne BiSAR imaging processing, the beam center crossing time is usually used as the azimuth focusing time to obtain the azimuth reference function. In STHM-BFSAR, however, the azimuth focusing time cannot be directly calculated form the geometric configuration because of the uncertainty of the azimuth direction. Therefore, the Doppler centroid is selected as the azimuth focusing position f_n. The difference of the Doppler centroid is used as a favorable factor to obtain the cross-range distribution of the target so as to avoid the influence of the spatial variation of Doppler centroid on the imagine focus quality. Based on the azimuth focusing position f_n, the azimuth reference function of the target in one range cell can be obtained for FNCS procedure.

Transforming (18) into the frequency domain by the MSR, the phase term is given by

$$\Phi_{az}\left(f_a\right) = \phi_2\left(f_a, f_n\right) + \phi_3\left(f_a, f_n\right) + \phi_4\left(f_a, f_n\right) \tag{19}$$

where $\phi_2(f_a, f_n)$, $\phi_3(f_a, f_n)$, and $\phi_4(f_a, f_n)$ are shown in Appendix A.

TABLE I
IMAGING PROCESSING TIME OF THREE METHODS

Method	Imaging Processing Time
BP	4.4328s
MRD	123.357ms
Proposed Method	177.958ms

TABLE II
SIMULATION PARAMETERS

Parameter	Value
Carrier Frequency	16GHz
PRF	10kHz
Range Bandwidth	100MHz
Range Sample Rate	120MHz
Synthetic Aperture Time	0.4s
Receiver's Velocity	(0,1000,-50)m/s
Receiver's Acceleration	(0,-100,50)m/s^2
Scene Center Location	(0,0,0)m
Transmitter Location	(-10,3,2)km
Initial Receiver Location	(0,-20,10)km

Observing (19), the compensation accuracy of $\phi_2(f_a, f_n)$ directly affects the azimuth focus, and the compensation accuracy of $\phi_3(f_a, f_n)$ and $\phi_4(f_a, f_n)$ is related to the side lobes of the focused image. In order to obtain a well-focused SAR image, these three spatial variant terms must be quantitatively analyzed before imaging processing to clarify their spatial variant characteristics. The spatial variant phase error of (19) is

$$\begin{cases} \Delta\phi_2 = \left|\phi_2\left(f_a, f_n\right) - \phi_2\left(f_a, 0\right)\right|_{f_a = B_a/2} \\ \Delta\phi_3 = \left|\phi_3\left(f_a, f_n\right) - \phi_3\left(f_a, 0\right)\right|_{f_a = B_a/2} \\ \Delta\phi_4 = \left|\phi_4\left(f_a, f_n\right) - \phi_4\left(f_a, 0\right)\right|_{f_a = B_a/2} \end{cases} \tag{20}$$

where B_a is the Doppler bandwidth, $\Delta\phi_2$, $\Delta\phi_3$, and $\Delta\phi_4$ are the spatial variant phase errors of $\phi_2(f_a, f_n)$, $\phi_3(f_a, f_n)$, and $\phi_3(f_a, f_n)$, respectively. Fig. 6 shows the spatial variant characteristics of phase error using the parameters in Table II. In SAR imaging processing, $\pi/4$ rad is often selected as the phase threshold. From the simulation results, the phase error caused by the spatial variation of $\phi_2(f_a, f_n)$ and $\phi_3(f_a, f_n)$ is much larger than $\pi/4$ rad, and the phase error caused by the spatial variation of $\phi_3(f_a, f_n)$ is much smaller than $\pi/4$ rad. Therefore, the spatial variant phase error of $\phi_2(f_a, f_n)$ and $\phi_3(f_a, f_n)$ cannot be ignored, and the spatial variant phase error of $\phi_4(f_a, f_n)$ is too small to affect the imaging quality, which can

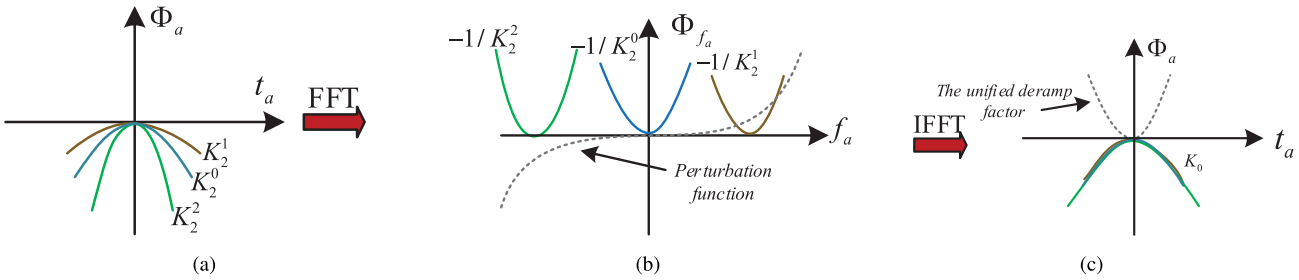

Fig. 7. Diagrams for the equalization of dependent Doppler coefficient. (a) The phase curves of three targets in the time domain. (b) The phase curves of three targets in the time domain and the FNCS operation. (c) The phase curves of the three targets with the same curvature in the time domain and the uniform deramp processing.

usually be ignored. After the nonspatial variant azimuth higher order phase is compensated and converted to the azimuth time domain, the echo signal becomes

$$S_4(\hat{t}, t_a) = \sin c\left(B_r\left(\hat{t} - R_{\text{bf0}}\right)\right) w_a(t_a) \cdot \exp\left(-j2\pi\frac{f_c}{c}K_1 t_a - j2\pi\frac{f_c}{c}K_2 t_a^2 - j2\pi\frac{f_c}{c}K_3 t_a^3\right). \tag{21}$$

2) Illustration of Modified FNCS: As previously analyzed, in the BiSAR spotlight mode imaging processing [43], the support regions of each point in the scene are overlapped in the time domain, but they are apart from each other in the frequency domain, which provided a theoretical basic for FNCS to perform in the frequency domain. Fig. 7 shows the Doppler parameters equalization process. Assuming that three different targets are located in the same range cell after range processing, the projections of their phase curves in the time domain are overlapped and have different curvatures because of the dependence of Doppler parameters. The curvatures of the phase curve of the three targets are K_2^1, K_2^0, and K_2^2 with $\text{abs}(K_2^1) < \text{abs}(K_2^0) < \text{abs}(K_2^2)$, as shown in Fig. 7(a). After the FFT on the variable t_a, the projection of the phase curve of different targets on the frequency axis is separated in the frequency domain. Therefore, we can introduce a higher order perturbation function in the frequency domain, whose function is to equalize the dependent Doppler parameters so that the curvature of the phase curve is the same, as shown in Fig. 7(b). Then, after the inverse FFT processing, the phase curves of the three targets are changed back to the time domain with the same curvature with the reference target. We can construct a unified azimuth focusing factor that is the conjugate of the phase of the reference target to achieve azimuth focusing processing, as shown in Fig. 7(c).

3) Derivation of Modified FNCS: The azimuth phase is more sensitive to errors than the envelope, so the range dependence of the Doppler parameters must be considered. The range dependence of the Doppler parameters is caused by the spatial variation of the Taylor expansion coefficient of the slant range. After polynomial fitting of Taylor expansion coefficients, as shown in (15), the range dependence of the Doppler parameter is eliminated.

Then we introduce a phase adjustment factor to first weaken the azimuth variation and provide sufficient coefficients for subsequent scaling operation. The phase adjustment factor is given as follows:

$$H_{\text{AD}}(t_a) = \exp\left(j\pi A t_a^3\right) \tag{22}$$

where A is the undetermined coefficient.

Multiplying (22) and (21) and transform it to the azimuth frequency domain through FFT, the azimuth phase is

$$\Phi_{ak}(f_a) = -\pi\frac{1}{f_{dr}}(f_a - f_n)^2 + \pi\frac{f_{dk} + A}{f_{dr}^3}(f_a - f_n)^3. \tag{23}$$

Here, we once again emphasize that the azimuth dependence of the Doppler parameters is caused by the different f_{dr} and f_{dk} of the target in the same range cell, which makes it impossible to perform the unified azimuth focusing processing. Usually f_{dr} and f_{dk} are approximated as a combination of a nonspatial variation term and a spatial variation term, where the nonspatial variation term is a constant and the spatial variation term is a polynomial of the azimuth focusing position f_n. So the approximation accuracy directly affects the compensation accuracy. The existing methods only approximate f_{dr} to the second order and f_{dk} to the first order, which is not sufficient in STHM-BFSAR because the presence of high speed and acceleration will cause the residual phase error to be greater $\pi/4$ rad. Therefore, for higher compensation accuracy and focusing effect, we approximate f_{dr} and f_{dk} to the second order as follows:

$$\begin{cases} f_{dr} \approx f_{dr0} + Bf_n + Cf_n^2 \\ f_{dk} \approx f_{dk0} + Ef_n + Ff_n^2 \end{cases} \tag{24}$$

where f_{dr0} and f_{dk0} are the Doppler FM rate and azimuth cubic coefficient of the scene center, respectively, B and C are the coefficients of first-order and second-order term of f_{dr} with respect to the azimuth focusing position f_n, and E and F are the coefficients of first-order and second-order terms of f_{dk} with respect to the azimuth focusing position f_n.

Figs. 8 and 9 show different orders approximation of the azimuth FM rate and azimuth cubic coefficient, and their corresponding approximation phase errors, respectively. It can be found that the second-order approximation matches the original azimuth FM rate and azimuth cubic coefficient much better than the first-order approximation, as shown in Figs. 8(a) and 9(a). Moreover, the second-order approximate phase errors of the azimuth modulation frequency and the azimuth cubic coefficient are both less than $\pi/4$ rad, compared with their first-order

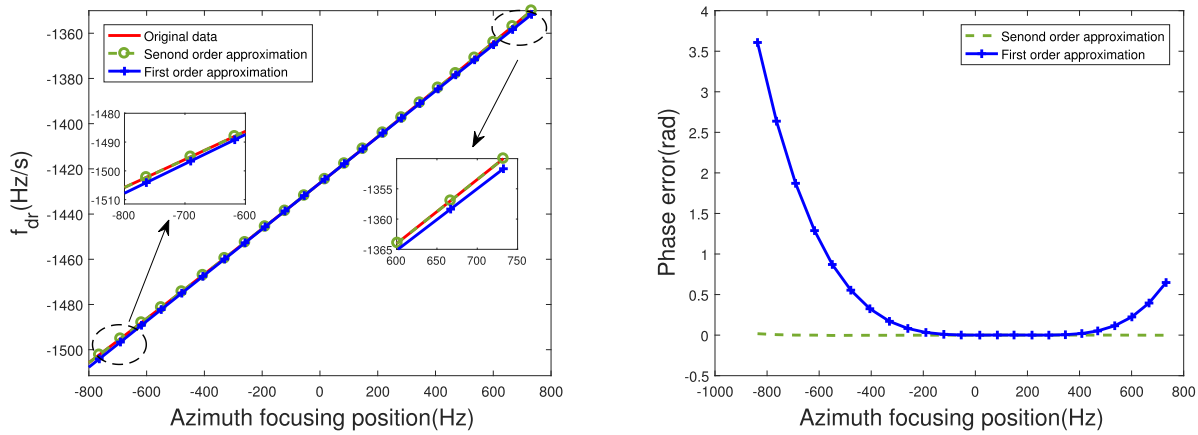

(a) (b)

Fig. 8. Diagrams for the azimuth FM rate approximation evaluation. (a) Azimuth FM rates for different order approximations. (b) Phase error induced by different approximated.

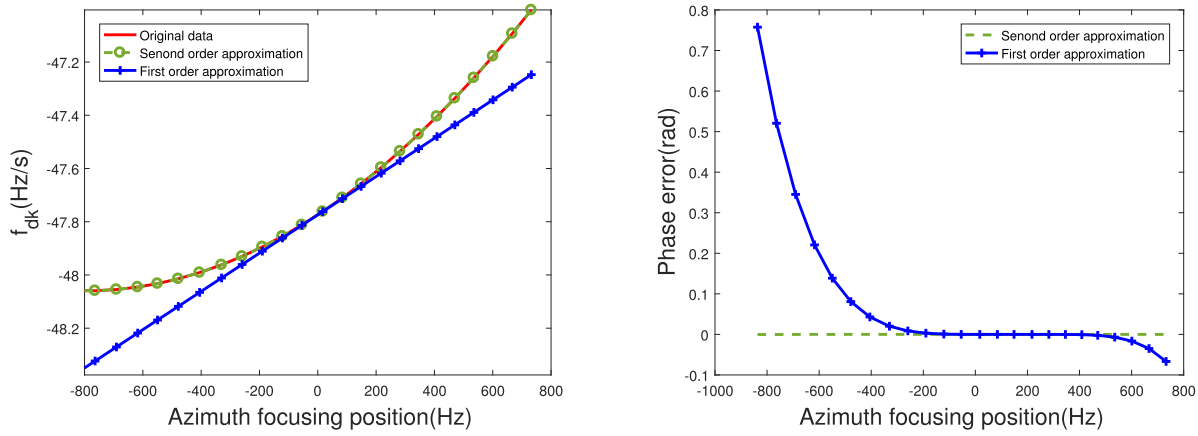

(a) (b)

Fig. 9. Diagrams for the azimuth cubic coefficient approximation evaluation. (a) Azimuth cubic coefficient for different order approximations. (b) Phase error induced by different approximated.

approximate phase errors greater than $\pi/4$ rad, as shown in Figs. 8(b) and 9(b). Thus, the second-order approximations of the azimuth FM rate and azimuth cubic coefficient are precise enough. However, the existing algorithm only adopts the first-order approximation of the azimuth cubic coefficient, which will limit the azimuth focus depth and raise the side lobes of the focused image due to the existence of the residual phase error.

Then, in order to eliminate the spatial variation of f_{dr} and f_{dk}, as analyzed previously, we introduce a fifth-order perturbation function to equalize the Doppler FM rate and the azimuth cubic phase coefficient in the frequency domain. The fifth-order perturbation function is

$$H_{\mathrm{AS}}(f_a) = \exp\left(j\pi \sum_{i=3}^{5} d_i f_a^i\right) \tag{25}$$

where d_3, d_4, and d_5 are the coefficients of the perturbation function.

Multiplying (23) by (25) and transforming the result into the time domain, then we have

$$\begin{aligned}\Phi_{at}\left(t_a; R_{\mathrm{bf0}}, f_n\right) = {} & 2\pi f_n t_a \\ & + \pi\varphi_1\left(R_{\mathrm{bf0}}\right) f_n^2 t_a \\ & + \pi\varphi_2\left(R_{\mathrm{bf0}}\right) f_n t_a^2 + \pi\varphi_3\left(R_{\mathrm{bf0}}\right) f_n^2 t_a^2 \\ & + \pi\varphi_4\left(R_{\mathrm{bf0}}\right) f_n t_a^3 + \pi\varphi_5\left(R_{\mathrm{bf0}}\right) f_n^2 t_a^3 \\ & + \pi\varphi_6\left(R_{\mathrm{bf0}}, t_a\right) + \pi\varphi_7\left(R_{\mathrm{bf0}}, f_n\right).\end{aligned} \tag{26}$$

Inspecting (26), the first term is the first-order coupling term between azimuth focusing position and the slow time, which represents the true azimuth frequency domain focusing position of the target. The second term represents the linear offset term of the azimuth position of the target caused by the NCS operation. The third and fourth terms are the first-order and second-order

spatial variation of the azimuth FM rate, respectively, which directly affect the azimuth focusing processing. The fifth and sixth terms are the first-order and second-order spatial variation of the cubic phase of the azimuth, respectively, which affect the side lobes of the focused image. The seventh term is the azimuth modulation term, which means the unified azimuth focusing term. The last term is a constant term, which has no effect on imaging and can be ignored.

In order to eliminate the azimuth variation of Doppler coefficients, these coefficients coupled with the azimuth frequency focusing position f_n should be set to zero, which yields

$$\begin{cases} \varphi_2\left(R_{\text{bf0}}\right) = 0 \\ \varphi_3\left(R_{\text{bf0}}\right) = 0 \\ \varphi_4\left(R_{\text{bf0}}\right) = 0 \\ \varphi_5\left(R_{\text{bf0}}\right) = 0. \end{cases} \tag{27}$$

Moreover, the related detailed expression is shown in Appendix B.

After the coupling between the Doppler coefficient and the azimuth focusing position f_n is eliminated, the dependent azimuth FM rate and the azimuth cubic coefficient have been equalized to be the same as the scene center, so we can construct the azimuth deramp factor (28), shown at the bottom of this page, to achieve the unified azimuth focusing processing.

Multiplying (26) with (28) and transforming the result into the azimuth frequency domain, then the final focused SAR image can be expressed as

$$S\left(\hat{t}, t_a\right) = \sin c\left(B_r\left(\hat{t} - \frac{R_{\text{bf0}}}{c}\right)\right) \cdot \sin c\left(\frac{1}{B_a}\left(f_a - f_n - \frac{3}{2} d_3 f_{dr0} f_n^2\right)\right). \tag{29}$$

C. Computation Cost

The high efficiency and real-time performance of calculations are particularly important for high maneuvering platforms. For engineering applications, this section analyzes the computational complexity of the algorithm. Suppose the number of samples in the azimuth and range directions are N_a and N_r, respectively. According to Fig. 5, the proposed algorithm only contains 2 times range FFT operations, 3 times azimuth FFT operations, 7 times multiplications, and a second-order KT operations that is completed by interpolation. The calculation amount of each azimuth or range FFT is $5N_rN_a\log_2(N_{r/a})$, the calculation amount of multiplications is $6N_rN_a$, and the calculation amount of interpolation is $2M(M-1)$, where M is the length of the interpolation kernel. Therefore, the total computational cost is

$$N_{\text{total}} = 10N_rN_a\log_2\left(N_r\right) + 15N_rN_a\log_2\left(N_a\right) + 42N_rN_a + 2\left(2M-1\right)N_rN_a. \tag{30}$$

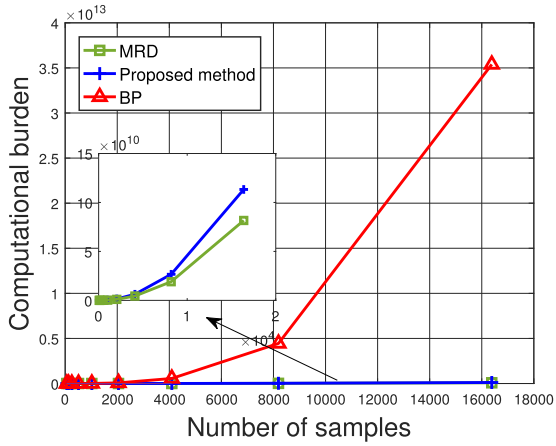

Fig. 10. Comparison of the computational complexity of three methods.

Assuming that the number of samples in the azimuth direction and the range direction are equal, that is, $N_r = N_a$, then the computational complexity of the proposed algorithm is $O(N^2\log_2(N))$. Consider the BP algorithm with the same number of samples in the range and azimuth, and its computational complexity is [44]

$$N_{\text{BP}} = 8N_aN_r^2 + \left(5M+5\right)N_rN_a\log_2\left(N_r\right) + \left[5M\log_2(M) + 6\right]N_rN_a. \tag{31}$$

Observation (31), the computational complexity of BP algorithm is (N^3). Obviously, the computational efficiency of the proposed algorithm is greatly improved compared with the BP algorithm. To demonstrate the real-time imaging performance of the proposed method, we also add the method in [42] as a comparison, which is a modified range Doppler (MRD) algorithm suitable for imaging of missile-borne high-speed platforms. The computational complexities of these three methods for different number of samples are simulated and shown in Fig. 10. We should note that the computational complexity of the proposed method is slightly higher than that of MRD due to the consideration of both RCM and the spatial variation of Doppler parameters. To further demonstrate the real-time imaging capability of the proposed method, we recorded the imaging time processed on the TMS320C6678 DSP, as given in Table I. The number of samples in the azimuth direction and the range direction are all equal to 2048. It can be seen from Table I that the imaging processing time of the proposed method is close to that of MRD. Furthermore, the imaging time of proposed method and MRD are all less than 500 ms, which is a limitation for real-time imaging processing of high maneuvering platforms with the size of 2048×2048. The previous analysis demonstrate

$$H_{\text{deramp}}\left(t_a\right) = \exp\left[\begin{array}{l} -j\pi f_{dr0}t_a^2 - j\pi\left(f_{9dk0} + A + d_3 f_{dr0}^3\right)t_a^3 - j\pi\left(d_4 f_{dr0}^4 + \frac{9}{2}d_3\left(f_{dk0}+A\right)f_{dr0}^2 + \frac{9\left(f_{dk0}+A\right)^2}{4f_{dr0}}\right)t_a^4 \\ -\pi d_5 f_{dr0}^5 t_a^5 \end{array}\right]. \tag{28}$$

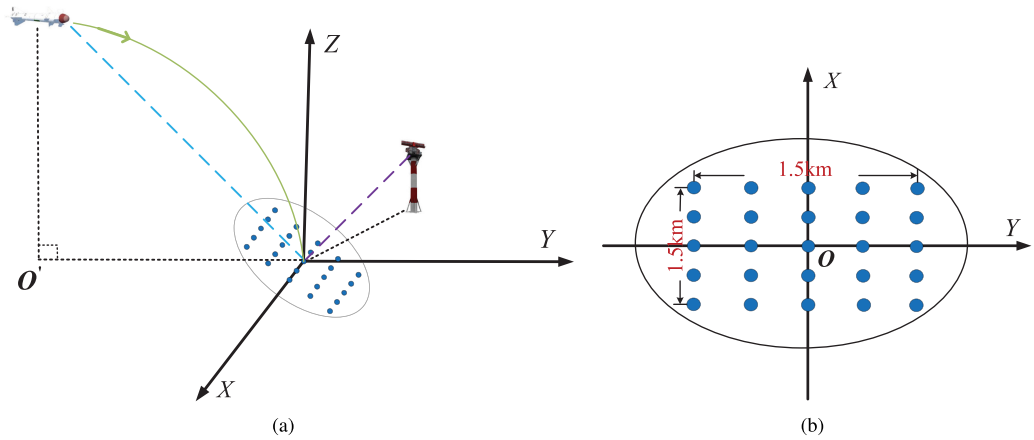

Fig. 11. Simulation geometry and target distribution. (a) Simulation geometry of STHM-BFSAR. (b) Target distribution.

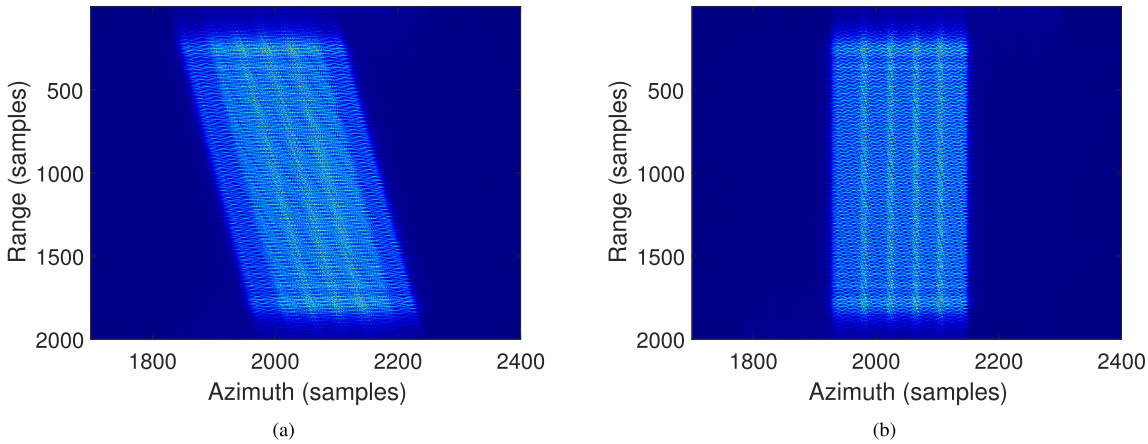

Fig. 12. Illustration of EKT performance in the proposed algorithm. (a) 2-D spectrum of original data. (b) 2-D spectrum of the echo after EKT operation.

the potential of the proposed method for real-time imaging and engineering applications.

D. Some Discussion

Compared with the stripmap mode, the Doppler bandwidth increase sharply in the spotlight mode due to the continuous illumination of the target scene by the beam. In order to prevent Doppler ambiguity, the PRF is usually very large, which causes a large computational load on high-speed maneuvering platform. Therefore, in order to meet the real-time requirements, the existence of Doppler ambiguity sometimes has to be allowed. In the case, it will not only result in the aliasing of the azimuth signal, but also cause the failure of EKT to correct the range walk of the targets because of the additional phase. Some effective methods [26], [45] are used to eliminate the aliasing of the azimuth spectrum through an azimuth prefiltering processing without affecting the structure of the imaging algorithm.

IV. Simulation Results

To verify the effectiveness and feasibility of the proposed algorithm, the simulation experiments based on the simulation parameters in Table II are shown in this section. In addition, in order to separately demonstrate the performance of the EKT-based RCMC and FNCS-based Doppler parameter equalization methods, the simulation is divided into three parts. The simulation selects a 5×5 uniform point array on the ground, the size is 1.5×1.5 km, and the distance between the two points is 375 m, as shown in Fig. 11(b).

A. Part I

The performance of EKT in the proposed algorithm is shown in this part. Fig. 12 illustrates the 2-D spectrum of simulated SAR data before and after EKT and the results after range compression. We can see that the spectrum before EKT is skewed due to severe range-azimuth coupling, as shown in Fig. 12(a). After EKT operation, the data are flattened, which indicates that the range-azimuth coupling is greatly alleviated, as shown in Fig. 12(b).

The residual RCM of the simulation points is shown in Fig. 13. After LRCMC, the scene edge points still have residual migration compared with the scene center points, as shown in Fig. 13(a). Fig. 13(b) shows the result of range compression after KT operation. KT eliminates the residual migration of the linear component by constructing the transformation factor, so

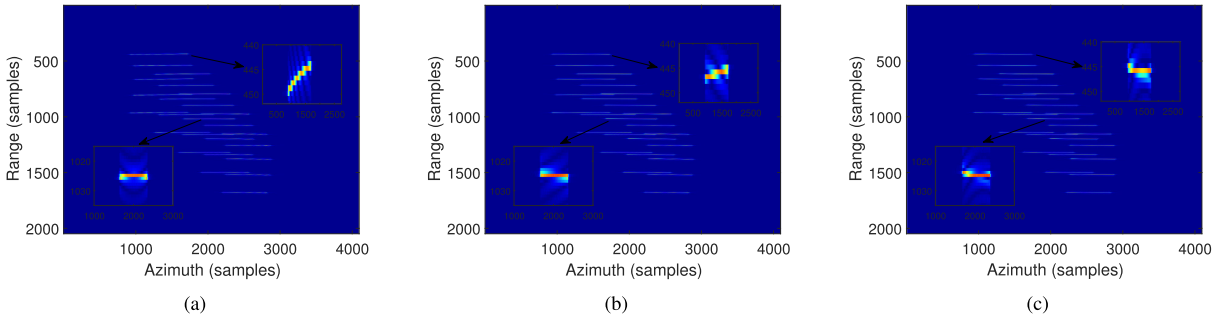

Fig. 13. Residual RCM of simulation points. (a) LRCMC. (b) KT. (c) EKT.

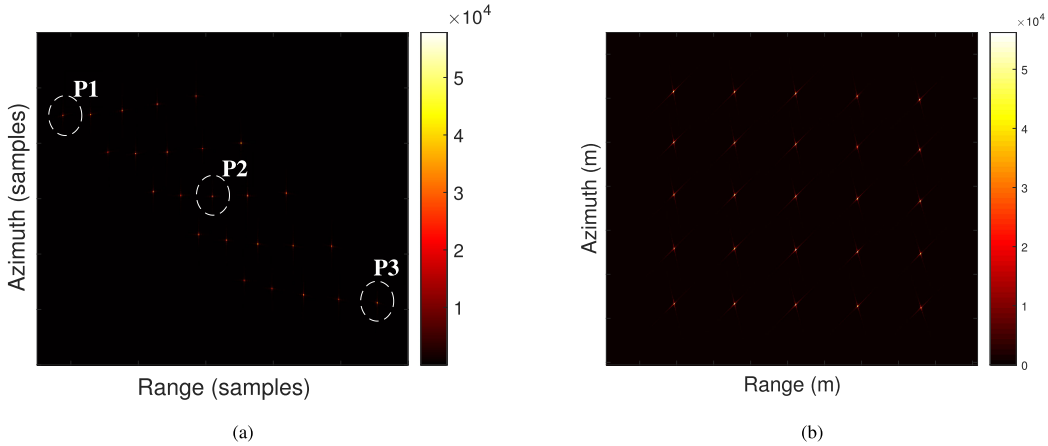

Fig. 14. Imaging results of the simulated points. (a) Imaging results before geometric correction. (b) Imaging result after geometric correction.

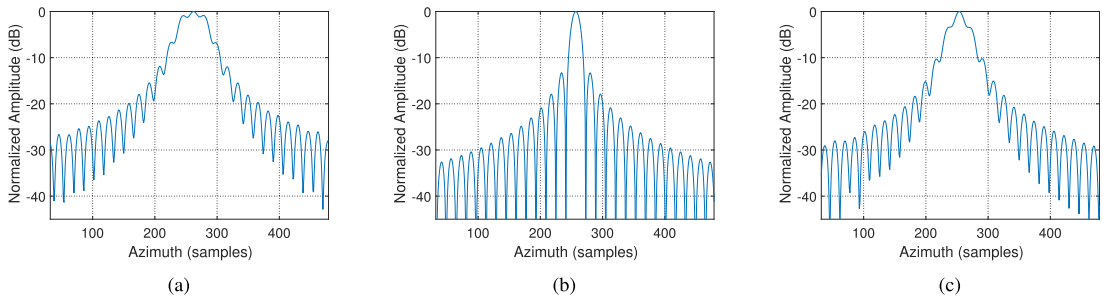

Fig. 15. Azimuth profiles of three points obtained by the basic method [22]. (a) Azimuth profiles of point P1. (b) Azimuth profiles of point P2. (c) Azimuth profiles of point P3.

the range compression result is greatly improved compared with LRCMC. However, the spatial variation of range curvature is ignored in STHM-BFSAR, the edge point still spans three range cells. The result of range compression after EKT operation is shown in Fig. 13(c). Each point target response is focused in the same range cell, even the energy of the edge point target is mainly located in one range cell, which provides convenience for subsequent processing and shows the good performance of EKT.

B. Part II

The performance of the FNCS-based Doppler parameter equalization is present in this part. Fig. 14 shows the imaging results of the simulated targets in the scene. All point targets, including the center point and edge points of the scene, are well focused by the modified FNCS. But due to EKT and NCS operations, the target position has an offset along the range and cross-range direction, which can be easily corrected by geometric correction methods [23]. The results after geometric correction for STHM-BFSAR are shown in Fig. 14(b), which can be used for target recognition and terminal guidance. In order to further prove the effectiveness of the proposed modified FNCS, the points marked P1, P2, and P3 in Fig. 14 are extracted for a comparison experiment to evaluate the focus quality in detail. Fig. 15 shows the azimuth impulse response profile of three points processed by the basic method [22]. Since the cross-range dependence characteristics of the azimuth FM rate and azimuth cubic coefficient are ignored, except for the scene center point

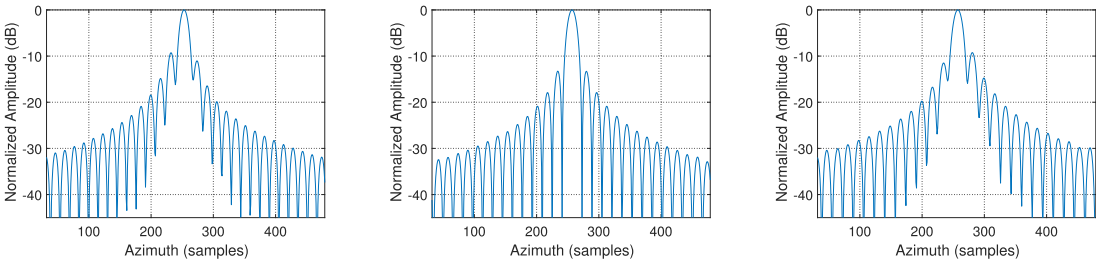

Fig. 16. Azimuth profiles of three points obtained by the reference method [37]. (a) Azimuth profiles of point P1. (b) Azimuth profiles of point P2. (c) Azimuth profiles of point P3.

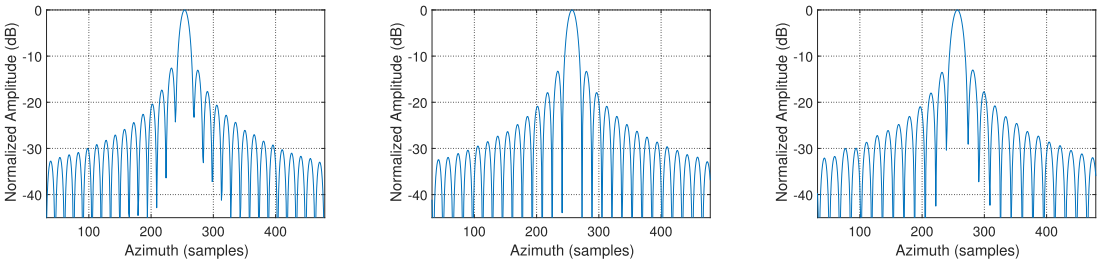

Fig. 17. Azimuth profiles of three points obtained by the proposed method. (a) Azimuth profiles of point P1. (b) Azimuth profiles of point P2. (c) Azimuth profiles of point P3.

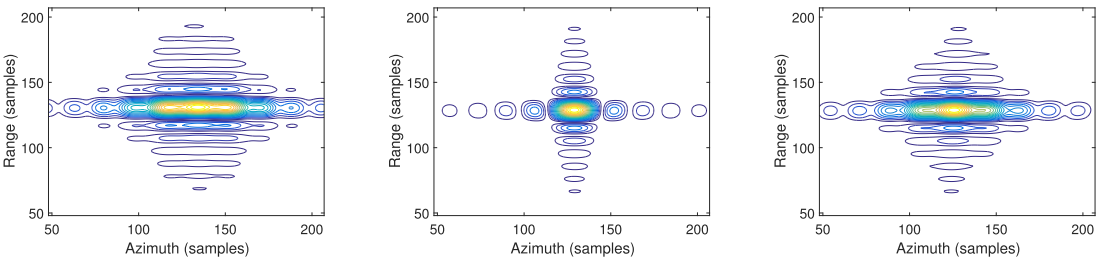

Fig. 18. Contour plots of three points obtained by the basic method [22]. (a) Contour plot of point P1. (b) Contour plot of point P2. (c) Contour plot of point P3.

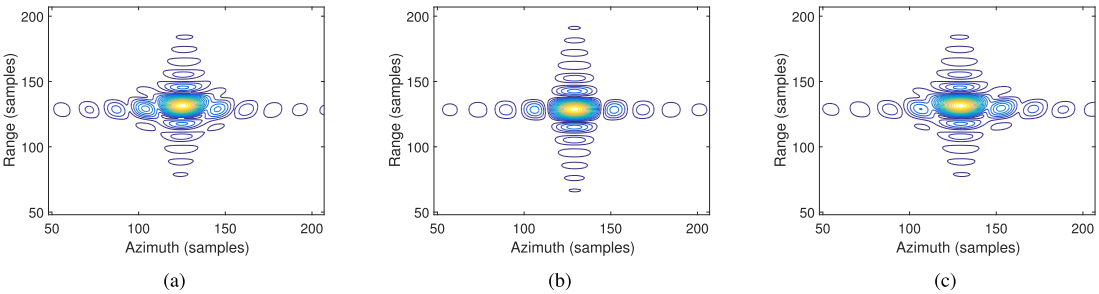

Fig. 19. Contour plots of three points obtained by the reference method [37]. (a) Contour plot of point P1. (b) Contour plot of point P2. (c) Contour plot of point P3.

P2, the other two points have very poor focusing effects, as shown in Fig. 15(a) and (c). The contour plots of the three points are also shown in Fig. 18 using the basic method. Compared with the basic method, the result of the reference method [37] has a great focus improvement because it takes the second-order spatial variation of the Doppler frequency and the first-order spatial variation of the azimuth cubic coefficient into consideration, as shown in Fig. 16. However, there is still a residual phase error that causes the side-lobes elevation and asymmetry of the edge point because the first-order approximation of the cubic phase coefficient of the method is not sufficient, as shown in Fig. 16(a) and (c). It is obvious that compared with the azimuth impulse

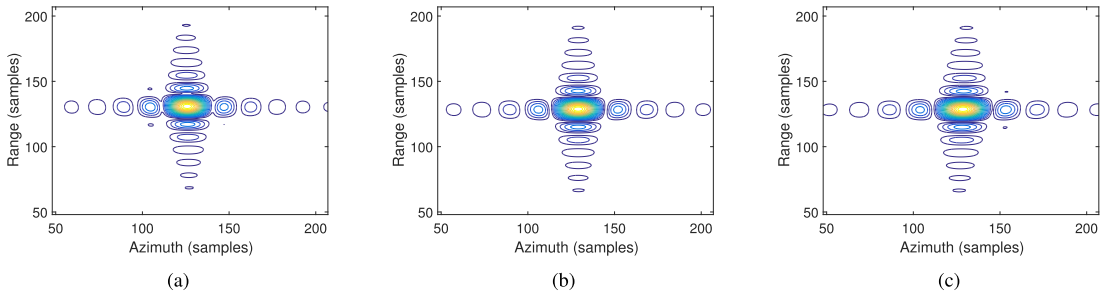

Fig. 20. Contour plots of three points obtained by the proposed method. (a) Contour plot of point P1. (b) Contour plot of point P2. (c) Contour plot of point P3.

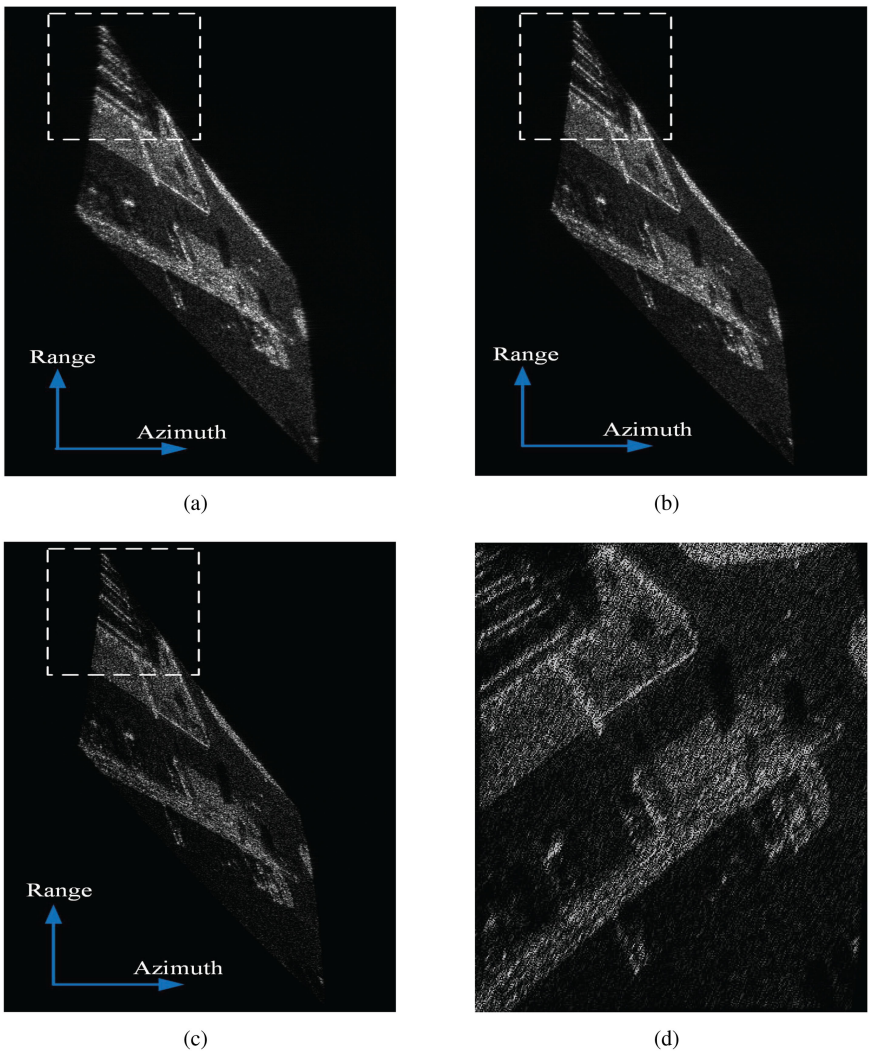

Fig. 21. Imaging results of scene simulation processed by the different methods. (a) Basic method. (b) Reference method. (c) Proposed method. (d) Geometric correction results of (c).

response profile of point P2, the results of point P1 and point P3 have obvious first side lobes and first zero point elevation and side lobes asymmetry. The contour plots of the three points are also shown in Fig. 19 using the reference method, which also has the problem of not separating the main lobes and side lobes at the edge points.

In comparison, the azimuth impulse response profile of the proposed algorithm is shown in Fig. 17. In the proposed method, since the second-order spatial variation of the azimuth FM rate and azimuth cubic coefficients are all eliminated, the residual phase error is smaller so that the azimuth profile of points P1 and P2 is closer to the center point of the scene P2, and compared with the reference method, since the second-order spatial variation of the cubic coefficients of the azimuth related to the side-lobes is considered, the first side lobes of point P1 and point P3 are significantly reduced, which proves the effectiveness of the

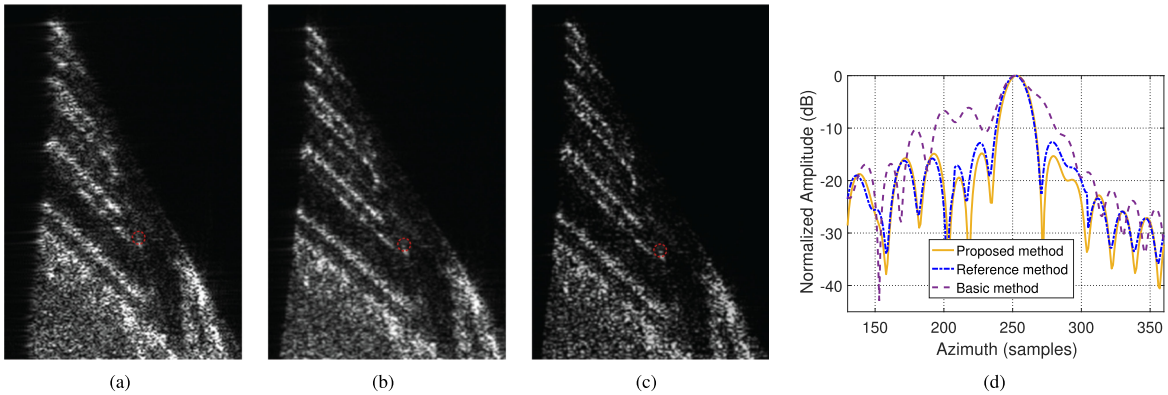

Fig. 22. Enlarged view of selected area in Fig. 19. (a) Basic method. (b) Reference method. (c) Proposed method. (d) Azimuth profiles of an isolated edge point obtained by the different method.

TABLE III
MEASURED PARAMETERS OF THE SELECTED POINTS

Method	Point	PSLR/dB	ISLR/dB
Basic Method	P1	N/A	N/A
	P2	-13.27	-10.26
	P3	N/A	N/A
Reference Method	P1	-8.58	-6.15
	P2	-13.27	-10.26
	P3	-9.95	-7.40
Proposed Method	P1	-13.13	-10.00
	P2	-13.27	-10.26
	P3	-12.65	-9.47

proposed algorithm. Fig. 20 gives the contour plots of three points using the proposed method, which demonstrates that the main lobes and side lobes are well separated with each other and present an ideal "cross." In addition, in order to further evaluate the imaging performance of the proposed algorithm, we choose peak side-lobe ratio (PSLR) and integrated side-lobe ratio (ISLR), which are commonly used in the field of SAR imaging, to calculate the size of the side lobes. The measured parameters, PSLR and ISLR, of the corresponding targets are listed in Table III. It can be found that the measurement parameters, PSLR and ISLR, of the proposed algorithm are the lowest due to the consideration of the nonlinear variation of the azimuth cubic coefficient related to the side lobes, which is nearly the theoretical values of -13 dB and -10 dB.

C. Part III

In order to further demonstrate the imaging performance of the proposed method in complex imaging scene, a scene target is simulated based on the true grayscale values of the benchmark SAR image. In the simulation, each pixel of the benchmark SAR image is regarded as a scattering point of the scene target. The intervals between each scattering point and the size of the image are 3 m and 1.5×1.5 km, respectively. Fig. 19 shows the results of scene simulation processed by the different method. The result of geometric correction for the proposed method is also shown in Fig. 19(d). It can be seen that the scattering characteristics of the benchmark SAR images are well displayed by the processing of the proposed method. Fig. 22 is an enlarged view of the white dashed area selected in Fig. 21. It is obvious that Fig. 22(a) is severely defocused, because the spatial variation of the Doppler parameter is not considered. In contrast, the imaging quality of the reference algorithm has been improved, but due to the existence of residual errors, the imaging performance is still not satisfactory, as shown in Fig. 22(b). The imaging result processed by the proposed algorithm has the best focusing performance because the second-order spatial variation of the azimuth FM rate and azimuth cubic coefficient is considered simultaneously, as shown in Fig. 22(c). For a more intuitive comparison, an isolated edge point in the red dashed circle is selected, and the corresponding azimuth profile via the three methods is shown in Fig. 22(d). The purple dash-dotted line is the azimuth profile of the basic method. Since the azimuth variance of the Doppler parameter is not considered, the main lobe is widened, and the side lobes are raised and asymmetrical. As shown by the blue dashed line, the side lobes are reduced processed by the reference method, and the resolution is improved, but PSLR and ISLR are still higher than the theoretical value due to the lack of azimuth focus depth. Because the proposed algorithm considers the second-order spatial variation of the azimuth cubic coefficient in STHM-BFSAR, there are lower side lobes for the edge points, which indicate a better focusing result. Therefore, the proposed method has a better scene edge focusing effect compared with the basic method and reference method. The theoretical derivation and imaging simulation evaluation all prove the effectiveness and feasibility of the proposed modified FNCS algorithm.

V. CONCLUSION

In this article, an imaging method based on EKT and modified FNCS for STHM-BFSAR data processing is proposed. First, the echo signal model for STHM-BFSAR is established, and the characteristics of the echo signal are analyzed in detail. Second, in order to eliminate the influence of acceleration, the preprocessing operation was done in the echo. Then, EKT was introduced to eliminate the spatial variation of RCM for alleviating the coupling of range and cross range, whose residual RCM is smaller compared with traditional KT. After range processing, the NCS is introduced in the frequency domain to

equalize dependent the Doppler parameters of targets in one range cell, which can eliminate the second-order spatial variation of the azimuth FM rate and azimuth cubic coefficient at the same time and reduce the side lobes of the focused image. Finally, the simulated results validate the effectiveness of the proposed method and the correctness of the analysis.

Appendix A

Equation (19) is the azimuth frequency domain signal by the MSR, and the corresponding coefficient expression is

$$f_n = -\frac{K_1}{\lambda} \tag{32}$$

$$\phi_2(f_a, f_n) = -\pi \frac{1}{f_{dr}(R_{\text{bf0}}, f_n)}(f_a - f_n)^2 \tag{33}$$

$$\phi_3(f_a, f_n) = \pi \frac{f_{dk}(R_{\text{bf0}}, f_n)}{f_{dr}^3(R_{\text{bf0}}, f_n)}(f_a - f_n)^3 \tag{34}$$

$$\phi_4(f_a, f_n) = \pi \frac{\left(\begin{array}{l} f_{dr}(R_{\text{bf0}}, f_n) f_{dm}(R_{\text{bf0}}, f_n) \\ -\frac{9}{4} f_{dk}^2(R_{\text{bf0}}, f_n) \end{array} \right)}{f_{dr}^5(R_{\text{bf0}}, f_n)}(f_a - f_n)^4. \tag{35}$$

Appendix B

After applying the NCS, the signal is (27), and the coefficients of phase are written by

$$\varphi_1(R_{\text{bf0}}) = 3d_3 f_{dr0} \tag{36}$$

$$\varphi_2(R_{\text{bf0}}) = B + 3d_3 f_{dr0}^2 \tag{37}$$

$$\varphi_3(R_{\text{bf0}}) = C + 6d_3 B f_{dr0} + \frac{9}{2} d_3 (f_{dk0} + A) + 6d_4 f_{dr0}^2 \tag{38}$$

$$\begin{aligned} \varphi_4(Rf_0) = {} & E + 3d_3 B f_{dr0}^2 + 9d_3 (f_{dk0} + A) f_{dr0} \\ & + 4d_4 f_{dr0}^3 \end{aligned} \tag{39}$$

$$\begin{aligned} \varphi_5(R_{\text{bf0}}) = {} & F + d_3 \left(3B^2 f_{dr0} + 3C f_{dr0}^2\right) + 12 d_4 B f_{dr0}^2 \\ & + 18 d_4 (f_{dk0} + A) f_{dr0} + 10 d_5 f_{dr0}^3 \\ & + 9 d_3 (E f_{dr0} + B f_{dk0} + AB) \end{aligned} \tag{40}$$

$$\begin{aligned} \varphi_6(R_{\text{bf0}}) = {} & \pi f_{dr0} t_a^2 + \pi \left(f_{dk0} + A + d_3 f_{dr0}^3\right) t_a^3 \\ & + \pi \left[\begin{array}{l} d_4 f_{dr0}^4 + \frac{9}{2} d_3 (f_{dk0} + A) f_{dr0}^2 \\ + \frac{9(f_{dk0} + A)^2}{4 f_{dr0}} \end{array} \right] t_a^4 \\ & + \pi d_5 f_{dr0}^5 t_a^5. \end{aligned} \tag{41}$$

Then, the analytic solution of the (28) is shown as

$$d_3 = -\frac{B}{3 f_{dr0}^2} \tag{42}$$

$$d_4 = \frac{E - 2C f_{dr0} + 3B^2}{8 f_{dr0}^3} \tag{43}$$

$$A = -\frac{2\left(C + 6 d_3 B f_{dr0} + \frac{9}{2} d_3 f_{dk0} + 6 d_4 f_{dr0}^2\right)}{9 d_3} \tag{44}$$

$$\begin{aligned} d_5 = {} & \\ & - \frac{\left(\begin{array}{l} F + 12 d_4 B f_{dr0}^2 + 9 d_3 (E f_{dr0} + B f_{dk0} + AB) + \\ d_3 \left(3B^2 f_{dr0} + 3C f_{dr0}^2\right) + 18 d_4 (f_{dk0} + A) f_{dr0} \end{array} \right)}{10 f_{dr0}^3}. \end{aligned} \tag{45}$$

Acknowledgment

The authors would like to thank the anonymous reviewers for their careful review and constructive comments.

References

[1] T. Zeng, Z. Wang, F. Liu, and C. Wang, "An improved frequency-domain image formation algorithm for mini-UAV-based forward-looking spotlight BiSAR systems," *Remote Sens.*, vol. 12, no. 17, Sep. 2020, Art. no. 2680.

[2] Z. Sun, J. Wu, Z. Li, H. An, and X. He, "Geosynchronous spaceborne-airborne bistatic SAR data focusing using a novel range model based on one-stationary equivalence," *IEEE Trans. Geosci. Remote Sens.*, vol. 59, no. 2, pp. 1214–1230, Feb. 2021.

[3] H. Zhong, Y. Zhang, Y. Chang, E. Liu, X. Tang, and J. Zhang, "Focus high-resolution highly squint SAR data using azimuth-variant residual RCMC and extended nonlinear chirp scaling based on a new circle model," *IEEE Geosci. Remote Sens. Lett.*, vol. 15, no. 4, pp. 547–551, Apr. 2018.

[4] S. Li, H. Zhong, C. Yang, H. Song, and X. Xu, "Focusing nonparallel-track bistatic SAR data using modified frequency extended nonlinear chirp scaling," *IEEE Geosci. Remote Sens. Lett.*, vol. 19, 2022, Art. no. 4007105, doi: 10.1109/LGRS.2020.3041508.

[5] D. An, X. Huang, T. Jin, and Z. Zhou, "Extended nonlinear chirp scaling algorithm for high-resolution highly squint SAR data focusing," *IEEE Trans. Geosci. Remote Sens.*, vol. 50, no. 9, pp. 3595–3609, Sep. 2012.

[6] X. Zhang, H. Gu, and W. Su, "Squint-minimized chirp scaling algorithm for bistatic forward-looking SAR imaging," *IET Radar Sonar Navig.*, vol. 14, no. 2, pp. 290–298, Feb. 2020.

[7] Q. Zhang, J. Wu, Z. Li, Y. Miao, and J. Yang, "PFA for bistatic forward-looking SAR mounted on high-speed maneuvering platforms," *IEEE Trans. Geosci. Remote Sens.*, vol. 57, no. 8, pp. 6018–6036, Aug. 2019.

[8] H. Zhong, R. Zhao, H. Song, M. Yang, and X. Xu, "An improved imaging algorithm for high-resolution and highly squinted one-stationary bistatic SAR using extended nonlinear chirp scaling based on equi-sum of bistatic ranges," *IEEE Geosci. Remote Sens. Lett.*, vol. 18, no. 7, pp. 1244–1248, Jul. 2020.

[9] M. Xing, H. Lin, and J. Chen, "A review of imaging algorithm in multi-plotform-borne synthetic aperture radar," *J. Radars*, vol. 8, no. 6, pp. 732–757, Dec. 2019.

[10] D. Liang, H. Zhang, Y. Cai, K. Liu, and K. Zhang, "An advanced phase synchronization scheme based on coherent integration and waveform diversity for bistatic SAR," *Remote Sens.*, vol. 13, no. 5, pp. 1–22, Mar. 2021.

[11] H. Li, R. Wang, and Y. Deng, "Analysis of time and beam synchronization errors for distributed spaceborne SAR," *J. Radars*, vol. 7, no. 2, pp. 244–253, Apr. 2018.

[12] H. Mei *et al.*, "Thorough understanding property of bistatic forward-looking high-speed maneuvering platform SAR," *IEEE Trans. Aerosp. Electron. Syst.*, vol. 53, no. 4, pp. 1826–1845, Aug. 2017.

[13] J. Wu, Z. Li, J. Yang, Y. Huang, and Q. Liu, "Focusing translational variant bistatic forward-looking SAR using extended nonlinear chirp scaling algorithm," in *Proc. IEEE Nat. Radar Conf.*, 2013, pp. 1–5.

[14] H. Deng, Y. Li, M. Liu, H. Mei, and Y. Quan, "A space-variant phase filtering imaging algorithm for missile-borne BiSAR with arbitrary configuration and curved track," *IEEE Sensors J.*, vol. 18, no. 8, pp. 3311–3326, Apr. 2018.

[15] C. Li, H. Zhang, and Y. Deng, "Focus improvement of airborne high-squint bistatic SAR data using modified azimuth NLCS algorithm based on lagrange inversion theorem," *Remote Sens.*, vol. 13, no. 10, May. 2021, Art. no. 1916.

[16] H. Zhong and X. Liu, "An extended nonlinear chirp-scaling algorithm for focusing large-baseline azimuth-invariant bistatic SAR data," *IEEE Geosci. Remote Sens. Lett.*, vol. 6, no. 3, pp. 548–552, Jul. 2009.
[17] T. Espeter, I. Walterscheid, J. Klare, A. R. Brenner, and J. Ender, "Bistatic forward-looking SAR experiments using an airborne receiver," in *Proc IEEE Int. Radar Symp.*, 2011, pp. 41–46.
[18] M. Rodriguez-Cassola, S. V. Baumgartner, G. Krieger, and A. Moreira, "Bistatic terraSAR-X/F-SAR spaceborne–airborne SAR experiment: Description, data processing, and results," in *IEEE Trans. Geosci. Remote Sens.*, vol. 48, no. 2, pp. 781–794, Feb. 2010.
[19] S. Zhou, L. Yang, L. Zhao, Y. Wang, and M. Xing, "A new fast factorized back projection algorithm for bistatic forward-looking SAR imaging based on orthogonal elliptical polar coordinate," *IEEE J. Sel. Top. Appl. Earth Observ. Remote Sens.*, vol. 12, no. 5, pp. 1508–1520, May 2019.
[20] D. Feng, D. An, and X. Huang, "An extended fast factorized back projection algorithm for missile-borne bistatic forward-looking SAR imaging," *IEEE Trans. Aerosp. Electron. Syst.*, vol. 54, no. 6, pp. 2724–2734, Dec. 2018.
[21] W. Pu, J. Wu, Y. Huang, J. Yang, and H. Yang, "Fast factorized back-projection imaging algorithm integrated with motion trajectory estimation for bistatic forward-looking SAR," *IEEE J. Sel. Top. Appl. Earth Observ. Remote Sens.*, vol. 12, no. 10, pp. 3949–3965, Oct. 2019.
[22] Y. Yuan, S. Chen, and H. Zhao, "An improved RD algorithm for maneuvering bistatic forward-looking SAR imaging with a fixed transmitter," *Sensors*, vol. 17, no. 5, May. 2017, Art. no. 1152.
[23] Z. Li *et al.*, "A frequency-domain imaging algorithm for highly squinted SAR mounted on maneuvering platforms with nonlinear trajectory," *IEEE Trans. Geosci. Remote Sens.*, vol. 54, no. 7, pp. 4023–4038, Jul. 2016.
[24] W. Wang, G. Liao, D. Li, and Q. Xu, "Focus improvement of squint bistatic SAR data using azimuth nonlinear chirp scaling," *IEEE Geosci. Remote Sens. Lett.*, vol. 11, no. 1, pp. 229–233, Jun. 2013.
[25] M. Liang, W. Su, and H. Gu, "Focusing high-resolution high forward-looking bistatic SAR with nonequal platform velocities based on keystone transform and modified nonlinear chirp scaling algorithm," *IEEE Sensors J.*, vol. 19, no. 3, pp. 901–908, Feb. 2019.
[26] Z. Wang, M. Liu, G. Ai, P. Wang, and K. Lv, "Focusing of bistatic SAR with curved trajectory based on extended azimuth nonlinear chirp scaling," *IEEE Trans. Geosci. Remote Sens.*, vol. 58, no. 6, pp. 4160–4179, Jun. 2020.
[27] J. Wu, Z. Li, Y. Huang, J. Yang, and Q. H. Liu, "An omega-k algorithm for translational invariant bistatic SAR based on generalized Loffeld's bistatic formula," *IEEE Trans. Geosci. Remote Sens.*, vol. 52, no. 10, pp. 6699–6714, Oct. 2014.
[28] Y. L. Neo, F. H. Wong, and I. G. Cumming, "A comparison of point target spectra derived for bistatic SAR processing," *IEEE Trans. Geosci. Remote Sens.*, vol. 46, no. 9, pp. 2481–2492, Sep. 2008.
[29] Y. L. Neo, F. H. Wong, and I. G. Cumming, "A two-dimensional spectrum for bistatic SAR processing using series reversion," *IEEE Geosci. Remote Sens. Lett.*, vol. 4, no. 1, pp. 93–96, Jan. 2007.
[30] L. Jing, S. Zhang, and J. Chang, "Bistatic forward-looking SAR imaging based on two-dimensional principle of stationary phase," in *Proc. Int. Workshop Microw. mm- Wave Circuits Syst. Technol.*, 2012, pp. 107–110.
[31] M. R. Cassola, G. Krieger, and M. Wendler, "Azimuth-invariant, bistatic airborne SAR processing strategies based on monostatic algorithms," in *Proc. IEEE Int. Geosci. Remote Sens. Symp.*, 2005, pp. 1047–1050.
[32] R. Wang, O. Loffeld, and H. Nies, "Image formation algorithm for bistatic forward-looking SAR," in *Proc. IEEE Int. Geosci. Remote Sens. Symp.*, 2010, pp. 4091–4094.
[33] C. Li, H. Zhang, Y. Deng, R. Wang, and Y. Zhang, "Focusing the L-band spaceborne bistatic SAR mission data using a modified RD algorithm," *IEEE Trans. Geosci. Remote Sens.*, vol. 58, no. 1, pp. 294–306, Jan. 2019.
[34] F. H. Wong, I. G. Cumming, and Y. L. Neo, "Focusing bistatic SAR data using the nonlinear chirp scaling algorithm," *IEEE Trans. Geosci. Remote Sens.*, vol. 46, no. 9, pp. 2493–2505, Sep. 2008.
[35] J. Wu, Z. Li, Y. Huang, and J. Yang, "Focusing bistatic forward-looking SAR with stationary transmitter based on keystone transform and nonlinear chirp scaling," *IEEE Geosci. Remote Sens. Lett.*, vol. 11, no. 1, pp. 148–152, Apr. 2014.
[36] J. Wu, Z. Sun, Z. Li, Y. Huang, J. Yang, and L. Zhe, "Focusing translational variant bistatic forward-looking SAR using keystone transform and extended nonlinear chirp scaling," *Remote Sens.*, vol. 8, no. 10, Oct. 2016, Art. no. 840.
[37] H. Mei, Y. Li, M. Xing, Y. Quan, and C. Wu, "A frequency-domain imaging algorithm for translational variant bistatic forward-looking SAR," *IEEE Trans. Geosci. Remote Sens.*, vol. 58, no. 3, pp. 1502–1515, Mar. 2020.
[38] X. Qiu, D. Hu, and C. Ding, "An improved NLCS algorithm with capability analysis for one-stationary BiSAR," *IEEE Trans. Geosci. Remote Sens.*, vol. 46, no. 10, pp. 3179–3186, Oct. 2008.
[39] L. Mu, W. Su, C. Ma, G. Hong, and J. Yang, "Focusing one-stationary bistatic forward-looking synthetic aperture radar based on squint minimization and modified nonlinear chirp scaling algorithm," *Int. J. Remote Sens.*, vol. 39, no. 22, pp. 7830–7845, Nov. 2018.
[40] Z. Li, J. Wu, W. Li, Y. Huang, and J. Yang, "One-stationary bistatic side-looking SAR imaging algorithm based on extended keystone transforms and nonlinear chirp scaling," *IEEE Geosci. Remote Sens. Lett.*, vol. 10, no. 2, pp. 211–215, Mar. 2013.
[41] C. Si, Y. Yue, S. Zhang, H. Zhao, and C. Yong, "A new imaging algorithm for forward-looking missile-borne bistatic SAR," *IEEE J. Sel. Top. Appl. Earth Observ. Remote Sens.*, vol. 9, no. 4, pp. 1543–1552, Apr. 2016.
[42] Z. Meng, Y. Li, M. Xing, and Z. Bao, "Imaging method for the extended scene of missile-borne bistatic forward-looking SAR," *J. Xidian Univ.*, vol. 43, no. 3, pp. 31–37, Jun. 2016.
[43] Y. Li, Z. Zhang, M. Xing, and Z. Bao, "Bistatic spotlight SAR processing using the frequency-scaling algorithm," *IEEE Geosci. Remote Sens. Lett.*, vol. 5, no. 1, pp. 48–52, Jan. 2008.
[44] Y. Guo, Z. Yu, J. Li, and C. Li, "Focusing spotlight-mode bistatic GEO-SAR with a stationary receiver using time-Doppler resampling," *IEEE Sensors J.*, vol. 20, no. 18, pp. 10766–10778, Sep. 2020.
[45] S. Tang, L. Zhang, P. Guo, G. Liu, and G. Sun, "Acceleration model analyses and imaging algorithm for highly squinted airborne spotlightmode SAR with maneuvers," *IEEE J. Sel. Top. Appl. Earth Observ. Remote Sens.*, vol. 8, no. 3, pp. 1120–1131, Mar. 2015.

Jiabao Ding (Student Member, IEEE) was born in Henan, China, in 1995. He received the B.S. degree in electronic engineering in 2018 from Xidian University, Xi'an, China, where he is currently working toward the Ph.D. degree in signal processing with the National Laboratory of Radar Signal Processing.

His research interests include bistatic SAR/ISAR imaging and bistatic ISAR distortion correction.

Yachao Li (Member, IEEE) was born in Jiangxi, China, in May, 1981. He received M.S. and Ph.D. degrees in electrical engineering in 2005 and 2008, respectively, from Xidian University, Xi'an, China.

He is currently a Professor with Xidian University. His current research interests include SAR/ISAR imaging, missile-borne SAR imaging, ground moving target indication (GMTI), matching and orientation of SAR image, real-time signal processing based on FPGA and DSP technology, and distributed radar.

Ming Li (Member, IEEE) was born in 1965. He received the B.S. degree in electrical engineering, and the M.S. and Ph.D. degrees in signal processing from Xidian University, Xi'an, China, in 1987, 1990, and 2007, respectively.

In 1987, he joined the Department of Electronic Engineering, Xidian University. He is currently a Professor with the National Laboratory of Radar Signal Processing, Xidian University. His research interests include adaptive signal processing, detection theory, ultrawide band, and SAR image processing.

Jiadong Wang received the B.S. degree in electronic and information engineering from Xidian University, Xi'an, China, in 2014, and the Ph.D. degree in signal processing from the National Laboratory of Radar Signal Processing, Xidian University, in 2020.

He is currently an Associate Professor with Xidian University. His research interests include radar signal processing, synthetic aperture radar, and inverse synthetic aperture radar imaging.